

# A Superior Bifunctional Electrocatalyst in Which Directional Electron Transfer Occurs Between a Co/Ni Alloy and Fe—N—C Support

Ziyi Xu, Shihao Wang, Wenmao Tu,\* Ling Shen, Lu Wu, Shilong Xu, Haining Zhang, Hongfei Pan,\* and Xiao-Yu Yang\*

**Stable, efficient, and economical bifunctional electrocatalysts for oxygen evolution reaction (OER) and oxygen reduction reaction (ORR) are needed for rechargeable Zn–air batteries. In this study, a directional electron transfer pathway is exploited in a spatial heterojunction of  $\text{Co}_y\text{Ni}_x@\text{Fe}-\text{N}-\text{C}$  heterogeneous catalyst for effective bifunctional electrolysis (OER/ORR). Thereinto, the Co/Ni alloy is strongly coupled to the Fe–N–C support through Co/Ni–N bonds. DFT calculations and experimental findings confirm that Co/Ni–N bonds play a bridging role in the directional electron transfer from Co/Ni alloy to the Fe–N–C support, increasing the content of pyridinic nitrogen in the ORR-active support. In addition, the discovered directional electron transfer mechanism enhances both the ORR/OER activity and the durability of the catalyst. The  $\text{Co}_{0.66}\text{Ni}_{0.34}@\text{Fe}-\text{N}-\text{C}$  with the optimal Ni/Co ratio exhibits satisfying bifunctional electrocatalytic performance, requiring an ORR half-wave potential of 0.90 V and an OER overpotential of 317 mV at 10 mA cm<sup>-2</sup> in alkaline electrolytes. The assembled rechargeable zinc–air batteries (ZABs) incorporating  $\text{Co}_{0.66}\text{Ni}_{0.34}@\text{Fe}-\text{N}-\text{C}$  cathode exhibits a charge–discharge voltage gap comparable to the Pt/C||IrO<sub>2</sub> assembly and high robustness for over 60 h at 20 mA cm<sup>-2</sup>.**

## 1. Introduction

The development of eco-friendly energy conversion and storage systems is a highly prioritized goal aimed at overcoming energy and environmental challenges.<sup>[1,2]</sup> Zn–Air batteries (ZABs) are traditionally employed in these systems because they have several advantageous features, such as high energy density, low cost, and high safety.<sup>[3–5]</sup> However, efficiencies of batteries of this type are highly dependent on the performance of catalysts for the OER (Oxygen Evolution Reaction) and the ORR (Oxygen Reduction Reaction) taking place at the air-cathode, which involve sophisticated concerted proton-electron transfer processes.<sup>[6–8]</sup> For example, the mismatched catalytic activity of traditional mono-functional Ir/Pt-based electrocatalysts for the OER and ORR limits the performance and raises the operational cost of ZABs.<sup>[9]</sup> Therefore, a critical need exists to develop new cost-effective bifunctional (OER/ORR) catalysts. Complexes of transition metal alloys that have favorable d-orbital electron occupancies and low costs, such as  $\beta$ -FeCo-PCNF and  $\text{Fe}_x\text{Ni}_y\text{N}@/\text{C}/\text{NC}$ ,

are good candidates for this purpose.<sup>[10,11]</sup> These alloys contain uniformly distributed metal atoms that are active for ORR and OER. However, the homogeneous atomic distribution confines electron transfer between consecutive metal atoms, resulting in protracted electron transfer and inferior electron utilization efficiency in the electrocatalytic reaction. The directional electron transfer within the heterogeneous components of the catalyst could shorten the electron transfer path and increase the electron utilization efficiency.

2D transition metal–nitrogen–carbon (M–N–C) materials, such as those containing Fe–N–C units, have high conductivities, favorable oxygen transport properties, and internal atomic scale electron-directed transfer abilities, all of which significantly boost their ORR performance.<sup>[12–14]</sup> Nonetheless, the OER activities of these materials are inferior due to inadequate OER active components and inefficient use of electrons.<sup>[15,16]</sup> Fortunately, CoNi alloys, which have intrinsic polarities, adjustable electronic structures, and excellent corrosion resistance in alkaline

---

Z. Xu, S. Wang, W. Tu, L. Shen, L. Wu, S. Xu, H. Zhang, X.-Y. Yang  
State Key Laboratory of Advanced Technology for Materials Synthesis and Processing

Wuhan University of Technology  
No. 122 Luoshi Road, Wuhan 430070, China  
E-mail: [tuwm@whut.edu.cn](mailto:tuwm@whut.edu.cn); [xyyang@seas.harvard.edu](mailto:xyyang@seas.harvard.edu)

Z. Xu, S. Wang, S. Xu, H. Zhang, H. Pan  
R&D Center of Materials and Stack Technology for Fuel Cell  
Foshan Xianhu Laboratory of the Advanced Energy Science and Technology  
Guangdong Laboratory

Foshan 528200, China  
E-mail: [panhongfei@whut.edu.cn](mailto:panhongfei@whut.edu.cn)

W. Tu  
Hubei Key Laboratory of Fuel Cell  
Wuhan University of Technology  
No. 122 Luoshi Road, Wuhan 430070, China

 The ORCID identification number(s) for the author(s) of this article can be found under <https://doi.org/10.1002/smll.202401730>

DOI: 10.1002/smll.202401730

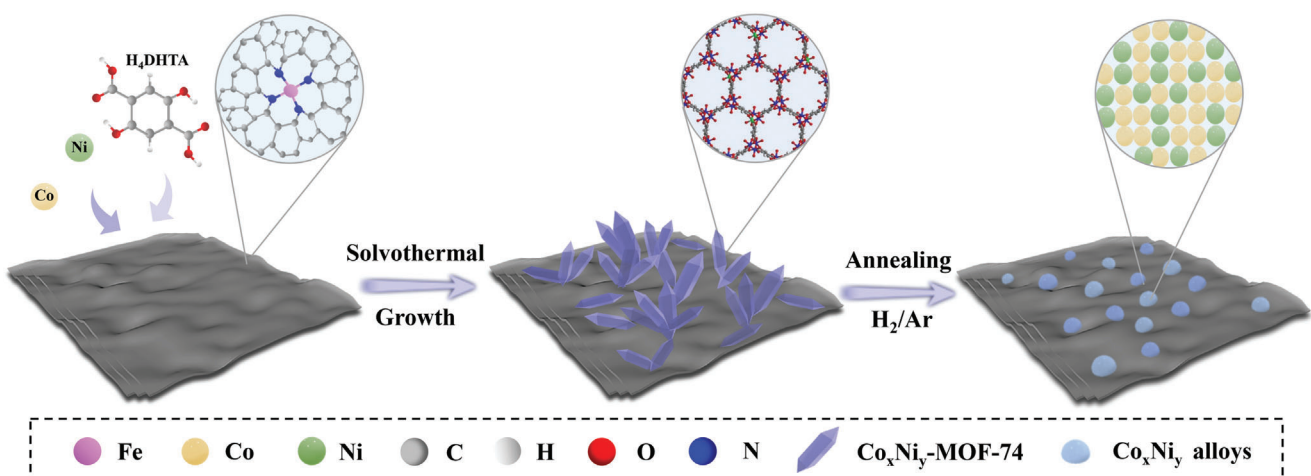


**Figure 1.** Schematic of the synthesis of  $\text{Co}_y\text{Ni}_x@$ Fe–N–C.

solutions, are generally utilized as non-precious metal components of bifunctional OER electrocatalysts.<sup>[17]</sup> In addition, CoNi alloys contain highly electronegative Co (1.88) and Ni (1.91) atoms, which can serve as electron donors to N-doped carbon that contains much less electronegative N (3.04) and C (2.55). Based on this, we propose that a directional electron transfer path would be created within the nano-scale heterojunction of CoNi alloy and M–N–C support due to the discrepancy of atomic electronegativity.

To assess the validity of this reasoning, we carry out an investigation to probe methods to create a hetero-structured material containing a spatial junction structure composed of CoNi alloy and Fe–N–C support and to determine its directional electron transfer ability as well as its performance as a bifunctional OER and ORR catalyst. In the study, we develop a new electronic beam transfer-based method to produce the hybrid material  $\text{Co}_y\text{Ni}_x@$ Fe–N–C, in which the  $\text{Co}_y\text{Ni}_x$  alloy (OER active) is strongly coupled to the Fe–N–C (ORR active) through the Co/Ni–N bond. X-ray photoelectron spectroscopy (XPS) and density functional theory (DFT) calculations confirm that a directional electron transfer pathway between the heterogeneous CoNi alloy and Fe–N–C support in this material, in which Co/Ni–N bonds play a bridging role in delivering electrons from CoNi alloy to Fe–N–C support, leading to increased pyridinic N species in the support. This unique directional electron transfer behavior in  $\text{Co}_y\text{Ni}_x@$ Fe–N–C contributes to superior ORR/OER bifunctional performance.  $\text{Co}_{0.66}\text{Ni}_{0.34}@$ Fe–N–C, with the optimal Co/Ni ratio, exhibits a half-wave potential ( $E_{1/2}$ ) of 0.90 V for ORR and an OER overpotential of only 317 mV to reach the current density of  $10 \text{ mA cm}^{-2}$  under alkaline conditions. A liquid zinc-air battery containing the synthesized composite shows excellent bifunctional catalytic activity for OER and ORR ( $\Delta E = 0.636 \text{ V}$ ) and a power density of  $182.7 \text{ mW cm}^{-2}$  at  $281.1 \text{ mA cm}^{-2}$ , which is superior to that of Pt/C || IrO<sub>2</sub> counterpart ( $127.8 \text{ mW cm}^{-2}$  at  $200.3 \text{ mA cm}^{-2}$ ). Results arising from this effort should encourage new studies aimed at designing new, cost-efficient, and strongly coupled hybrid bifunctional ORR/OER nanomaterials to replace benchmark catalysts (Pt, Ir/Ru-based materials) for application in various energy technologies.

## 2. Results and Discussion

### 2.1. Materials Synthesis and Characterization

The procedure for the synthesis of  $\text{Co}_y\text{Ni}_x@$ Fe–N–C is shown in **Figure 1**. In the route, the Fe–N–C support was prepared by pyrolysis of a mixture of melamine and hemin chloride (Figure S1a, Supporting Information). A complex containing different amounts of  $\text{Co}^{2+}$  and  $\text{Ni}^{2+}$  coordinated to the aryloxide and carboxylate groups of 2,5-dioxido-1,4-benzenedicarboxylate ( $\text{H}_4\text{DOBDC}$ ) was incorporated into Fe–N–C via a solvothermal process to form  $\text{Co}_y\text{Ni}_x$ -MOF-74@Fe–N–C containing varying ratios of Co and Ni as precursors. The SEM image (Figure S1b, Supporting Information) and X-ray diffraction (XRD) patterns (Figure S2, Supporting Information) demonstrate that the solvothermal process does indeed generate a material in which  $\text{Co}_y\text{Ni}_x$ -MOF-74 is located on the Fe–N–C support. The XRD patterns of  $\text{Co}_y\text{Ni}_x$ -MOF-74@Fe–N–C with varying Ni/Co ratios show diffraction peaks consistent with that of simulated MOF-74, indicating that the crystal phase of MOF-74 is well retained with varying Ni/Co ratios. The diffraction peaks in the XRD pattern at  $6.9^\circ$  and  $11.9^\circ$  are assigned to the (210) and (300) planes of MOF-74, respectively, while the broad peak at  $20^\circ$ – $30^\circ$  corresponds to an amorphous carbon structure.<sup>[18]</sup>

The  $\text{Co}_y\text{Ni}_x$ -MOF-74@Fe–N–C materials with varying Ni/Co ratios were pyrolyzed under  $\text{H}_2/\text{Ar}$  atmosphere and transformed into a series of  $\text{Co}_y\text{Ni}_x$ @Fe–N–C catalysts, including  $\text{Co}$ -MOF-74@Fe–N–C, Ni-MOF-74@Fe–N–C,  $\text{Co}_{0.76}\text{Ni}_{0.24}$ -MOF-74@Fe–N–C,  $\text{Co}_{0.66}\text{Ni}_{0.34}$ -MOF-74@Fe–N–C,  $\text{Co}_{0.50}\text{Ni}_{0.50}$ -MOF-74@Fe–N–C,  $\text{Co}_{0.34}\text{Ni}_{0.66}$ -MOF-74@Fe–N–C and  $\text{Co}_{0.24}\text{Ni}_{0.76}$ -MOF-74@Fe–N–C. The Ni/Co mole ratios in these materials were determined using inductively coupled plasma-atomic emission spectrometry (ICP-AES) (Tables S1 and S2, Supporting Information). The XRD patterns of  $\text{Co}_y\text{Ni}_x$ @Fe–N–C with different Ni/Co ratios are shown in Figure S3 (Supporting Information). The broad peaks present between  $20^\circ$  and  $30^\circ$  are attributed to the amorphous carbon support, and peaks at  $44.5^\circ$ ,  $51.8^\circ$ , and  $76.3^\circ$  correspond to CoNi alloy (111), (200), and (220) planes, respectively. It is worth noting that the peak intensity

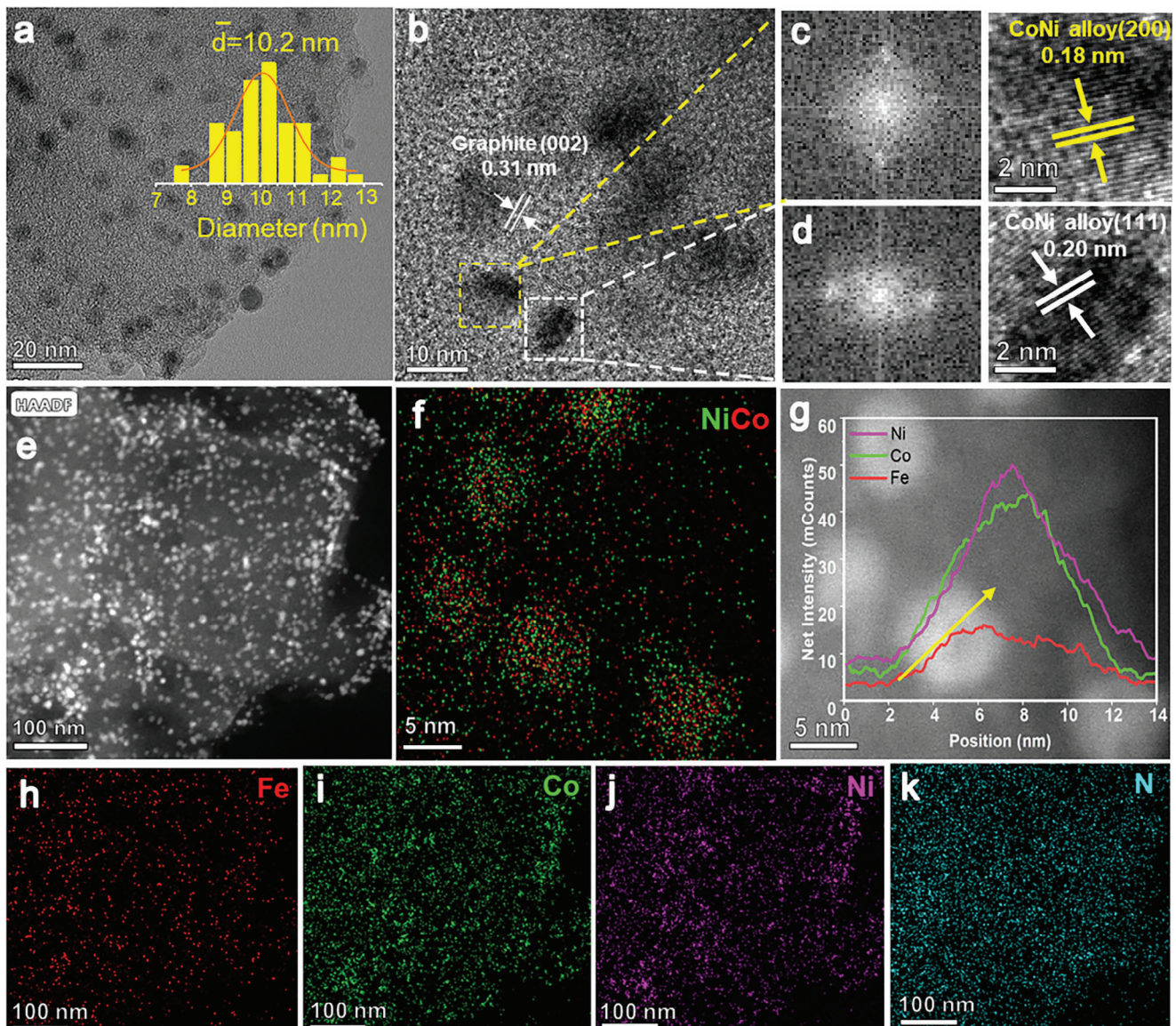


**Figure 2.** Observation of spatial junction consisting of CoNi embedded in the Fe–N–C support. a,b) HR-TEM image of  $\text{Co}_{0.66}\text{Ni}_{0.34}$ @Fe–N–C. c,d) HR-TEM image of  $\text{Co}_{0.66}\text{Ni}_{0.34}$ @Fe–N–C by Fast Fourier Transform and inverse Fast Fourier Transform. e,h–k) HAADF-STEM image and EDX mappings of  $\text{Co}_{0.66}\text{Ni}_{0.34}$ @Fe–N–C. f) EDX mapping image, and g) intensity profile of line scanning for CoNi alloy nanoparticles in  $\text{Co}_{0.66}\text{Ni}_{0.34}$ @Fe–N–C.

of the alloy is decreased with the reduction of Ni/Co ratios, indicating that alloy crystallinity can be reduced by introducing Co.<sup>[19]</sup>

As shown in Figure S1c (Supporting Information),  $\text{Co}_y\text{Ni}_x$ -MOF-74 crystals on Fe–N–C in  $\text{Co}_y\text{Ni}_x$ -MOF-74@Fe–N–C are transformed into uniform metal nanoparticles. Moreover, the XRD patterns (Figure S3, Supporting Information) confirm that the CoNi alloy present in  $\text{Co}_y\text{Ni}_x$ -MOF-74@Fe–N–C is not contaminated with any Fe-based compounds. In Figure 2a, the TEM image of  $\text{Co}_{0.66}\text{Ni}_{0.34}$ @Fe–N–C shows CoNi alloy nanoparticles with an average size of ca. 10.2 nm are uniformly distributed on the Fe–N–C support. The control samples with different Co/Ni ratios also display the consistent size of alloy nanoparticles (Figure S4, Supporting Information). This observation suggests

that MOF-derived carbon, in combination with the Fe–N–C support, can prevent the aggregation of nanoparticles and confine their sizes during the pyrolysis process. As shown in Figure 2b, the HR-TEM image of  $\text{Co}_{0.66}\text{Ni}_{0.34}$ @Fe–N–C indicates that CoNi alloy nanoparticles are embedded in graphite. The lattice fringe with spacings of 0.31, 0.20, and 0.18 nm corresponds to the (002) plane of graphite, (111), and (200) planes of CoNi alloy, respectively (Figure 2c,d).<sup>[20,21]</sup> The strong overlap of Ni and Co elements in energy dispersive X-ray (EDX) mapping (Figure 2f) and line scanning analysis (Figure 2g) further demonstrates that the CoNi alloy is formed after the pyrolysis of  $\text{Co}_{0.66}\text{Ni}_{0.34}$ -MOF-74@Fe–N–C precursor. Moreover, the HAADF-STEM and corresponding EDX mapping images reveal that Fe and N elements are uniformly distributed in  $\text{Co}_{0.66}\text{Ni}_{0.34}$ @Fe–N–C

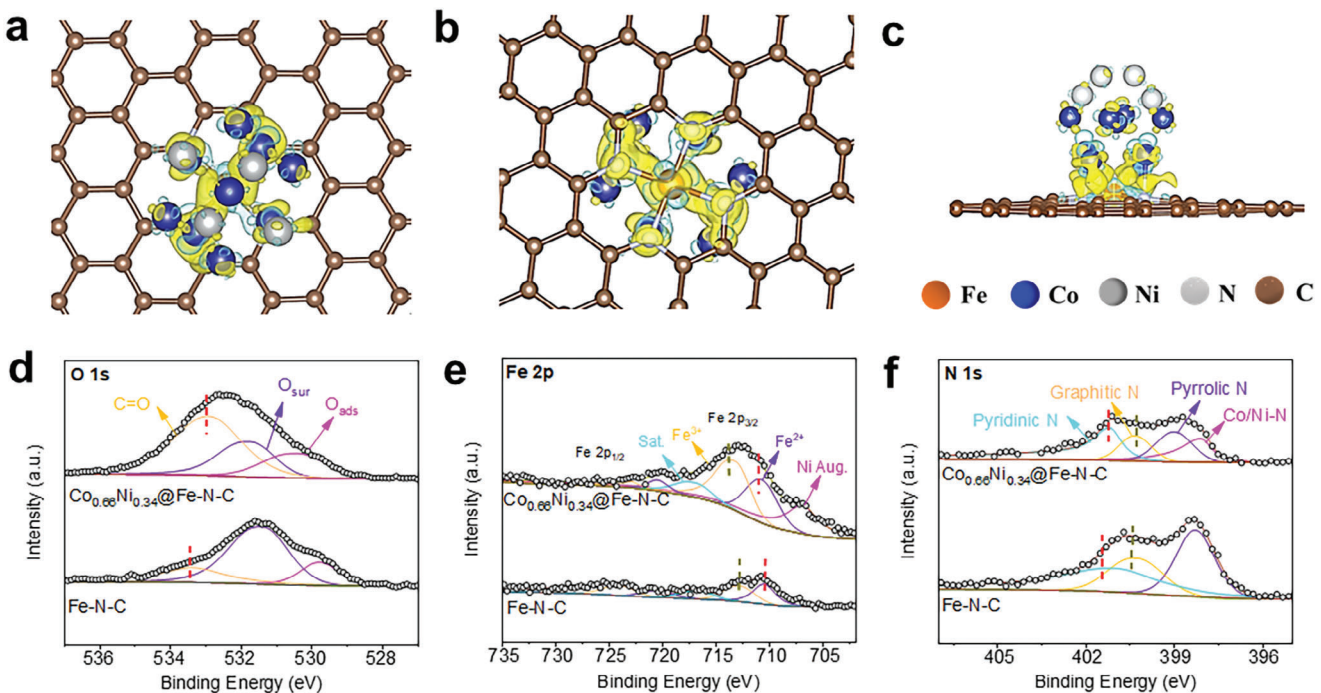


**Figure 3.** DFT calculated structures and charge densities of  $\text{Co}_{0.66}\text{Ni}_{0.34}@\text{Fe}-\text{N}-\text{C}$  viewed from a) vertical, b) bottom, and c) front view. Yellow and blue regions represent positive (electron accumulation) and negative (electron depletion) values, respectively. Element chemical state, from high-resolution XPS spectra of  $\text{Co}_{0.66}\text{Ni}_{0.34}@\text{Fe}-\text{N}-\text{C}$ ,  $\text{Ni}@\text{Fe}-\text{N}-\text{C}$ , and  $\text{Fe}-\text{N}-\text{C}$  in the d) O 1s, e) Fe 2p and f) N 1s regions.

(Figure 2e,h–k). Compared to the HAADF-STEM and EDX mapping images of  $\text{Fe}-\text{N}-\text{C}$ , the CoNi alloy nanoparticles embedded in the  $\text{Fe}-\text{N}-\text{C}$  support can be clearly identified in  $\text{Co}_{0.66}\text{Ni}_{0.34}@\text{Fe}-\text{N}-\text{C}$ , leading to an intimate heterostructure (Figure S5, Supporting Information).

The nitrogen adsorption-desorption experiments for  $\text{Fe}-\text{N}-\text{C}$ ,  $\text{Co}@\text{Fe}-\text{N}-\text{C}$ ,  $\text{Ni}@\text{Fe}-\text{N}-\text{C}$ ,  $\text{Co}_{0.66}\text{Ni}_{0.34}@\text{C}$ , and  $\text{Co}_{0.66}\text{Ni}_{0.34}@\text{Fe}-\text{N}-\text{C}$  displayed in Figure S6 (Supporting Information) show that the specific surface areas for the respective materials are 1057, 841, 516, 169, and  $671 \text{ m}^2 \text{ g}^{-1}$ , respectively.<sup>[22]</sup> This indicates that  $\text{Fe}-\text{N}-\text{C}$  has an extremely high specific surface area, and the increase in surface area is attributed to  $\text{Fe}-\text{N}-\text{C}$  rather than MOF-74 or MOF-74-derived C (Figure S7, Supporting Information). Besides, the mesopore structure of  $\text{Co}_y\text{Ni}_x@\text{Fe}-\text{N}-\text{C}$  increases upon the inclusion of MOF-74, which generates more mass transport channels (Figures S8 and S9, Supporting Information). The specific surface area of  $\text{Co}_{0.66}\text{Ni}_{0.34}@\text{Fe}-\text{N}-\text{C}$  is slightly smaller than that of  $\text{Co}@\text{Fe}-\text{N}-\text{C}$  and larger than that of  $\text{Ni}@\text{Fe}-\text{N}-\text{C}$ , which is consistent with the fact that Ni has a weaker binding strength with ligands in comparison with Co. This makes it easier to separate from the MOF-74 framework, where Ni tends to agglomerate into large particles during high-temperature pyrolysis.<sup>[20]</sup>

Due to the large difference of electronegativity between the Co (1.88), Ni (1.91), N (3.04), and C (2.55) elements in  $\text{Co}_{0.66}\text{Ni}_{0.34}@\text{Fe}-\text{N}-\text{C}$ , the N and C in the support should be more effective in capturing electrons from the CoNi alloy. This prediction is validated by DFT calculations on a model composed of CoNi alloy and  $\text{Fe}-\text{N}-\text{C}$  support connected through

the Co/Ni–N bond (Figure S10, Supporting Information). The results show that a significant enrichment of electrons on the  $\text{Fe}-\text{N}-\text{C}$  support (yellow section in Figure 3a–c) and a major region of charge depletion surrounds the CoNi alloy (blue section) at the interface of the heterostructure, verifying that electrons can be transferred directionally from the CoNi alloy to the N-doped carbon support in this material.<sup>[23,24]</sup> Additional information about this conclusion comes from the characterization of directional electron transfer in  $\text{Co}_{0.66}\text{Ni}_{0.34}@\text{Fe}-\text{N}-\text{C}$  using XPS. The survey spectrum (Figure S11, Supporting Information) shows that Co, Fe, Ni, C, N, and O elements are present in  $\text{Co}_{0.66}\text{Ni}_{0.34}@\text{Fe}-\text{N}-\text{C}$ . The high-resolution C 1s spectrum for this material was deconvoluted into C–C, C–N, C–O, and O–C=O components (Figure S12, Supporting Information).<sup>[25]</sup> As C is usually used to calibrate samples, it is not easy to evaluate shifts of C 1s peaks. The O peak from the  $\text{Fe}-\text{N}-\text{C}$  supports was chosen to determine the extent of directional electron transfer from CoNi alloys to the carbon supports. Analysis of the peak arising from O in the carbon supports shows that the O 1s peak in the spectrum of  $\text{Co}_{0.66}\text{Ni}_{0.34}@\text{Fe}-\text{N}-\text{C}$  is negatively shifted by 0.6 eV (Figure 3d) in comparison with  $\text{Fe}-\text{N}-\text{C}$ , suggesting that the electron density in the carbon support is increased due to the directional electron transfer from the CoNi alloy to the  $\text{Fe}-\text{N}-\text{C}$  support,<sup>[26]</sup> which is consistent with the results of DFT calculations. Four deconvoluted peaks are present in the N 1s XPS spectra of  $\text{Co}_{0.66}\text{Ni}_{0.34}@\text{Fe}-\text{N}-\text{C}$  and  $\text{Fe}-\text{N}-\text{C}$  (Figure 3f) at 398.2, 399.1, 400.9, and 402.1 eV, which correspond to Co/Ni–N, pyrrolic N, graphitic N, and pyridinic N, respectively.<sup>[27]</sup> The respective 0.5 eV and 0.3 eV negative shifts of pyridinic N and graphitic N peaks further indicate that the electron density of

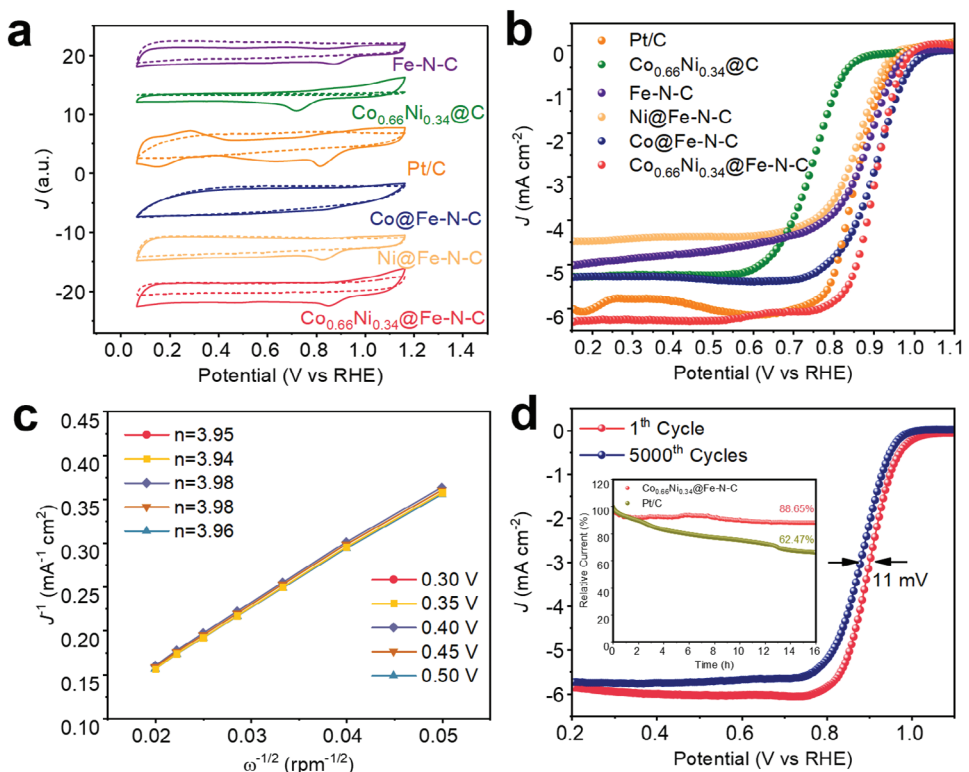


**Figure 4.** Evaluation of the bifunctional electrocatalytic ORR performance. a) CV curves in  $\text{N}_2$  (dashed line) and  $\text{O}_2$ -saturated (solid line) 0.1 M KOH solutions. b) LSV curves for ORR in  $\text{O}_2$ -saturated 0.1 M KOH solution at 1600 rpm. c) Koutecky–Levich plots and numbers of electrons transferred at different potentials for  $\text{Co}_{0.66}\text{Ni}_{0.34}@\text{Fe}-\text{N}-\text{C}$ . d) Stability test for the ORR.

support N atoms is increased in  $\text{Co}_{0.66}\text{Ni}_{0.34}@\text{Fe}-\text{N}-\text{C}$ . In addition, the content of graphitic N is significantly decreased by 6.8% and that of the pyridinic N is increased by 6.0% (Table S5, Supporting Information), indicating that CoNi nanoparticles coordinate mainly with graphitic N in the supports to function as a bridge for electron transfer, and that electrons eventually move to the pyridinic N sites. The pyrrolic N away from the directional electron transfer center exhibits decreased electron density due to electroneutrality. Therefore, pyrrolic N shows a positive shift in the binding energy after incorporating CoNi alloy. Moreover, the contents of pyrrolic N decreases, mainly due to the interaction between pyrrolic N and CoNi alloy.

Furthermore, the  $\text{Co}_{0.66}\text{Ni}_{0.34}@\text{Fe}-\text{N}-\text{C}$  catalyst exhibits binding energies for  $\text{Fe}^{2+}$   $2\text{p}_{3/2}$  (710.5 eV) and  $\text{Fe}^{3+}$   $2\text{p}_{3/2}$  (712.9 eV), which are lower than the 710.9 and 713.6 eV for  $\text{Fe}^{2+}$   $2\text{p}_{3/2}$  and  $\text{Fe}^{3+}$   $2\text{p}_{3/2}$  of  $\text{Fe}-\text{N}-\text{C}$ , respectively (Figure 3e). There is no signal associated with metallic  $\text{Fe}^0$  in the spectra of these materials.<sup>[28]</sup> The results show that electrons directly transfer from Fe to nearby N and C atoms in the  $\text{Fe}-\text{N}-\text{C}$  plane in  $\text{Co}_{0.66}\text{Ni}_{0.34}@\text{Fe}-\text{N}-\text{C}$  owing to the much smaller electronegativity of Fe (1.83) compared to those of N (3.04) and C (2.55). Compared to  $\text{Co}_{0.66}\text{Ni}_{0.34}@\text{C}$ , the Ni 2p spectrum of  $\text{Co}_{0.66}\text{Ni}_{0.34}@\text{Fe}-\text{N}-\text{C}$  is shifted to higher binding energy by 0.2 eV (Figure S13, Supporting Information), indicating that the directional electron loss propensity of Ni is modulated by the  $\text{Fe}-\text{N}-\text{C}$  sites. Compared to that of  $\text{Co}@\text{Fe}-\text{N}-\text{C}$ , the Co  $2\text{p}_{3/2}$  spectrum of  $\text{Co}_{0.66}\text{Ni}_{0.34}@\text{Fe}-\text{N}-\text{C}$  shows a new peak at 778.4 eV attributed to  $\text{Co}^0$  (Figure S14, Supporting Information). From

this observation, it could also be deduced that the temperature at which Co is transformed to its zero-valent state is reduced by alloying with Ni.

Results arising from both the DFT calculations and XPS studies described above lead to the same conclusion that directed electron transfer occurs in  $\text{Co}_{0.66}\text{Ni}_{0.34}@\text{Fe}-\text{N}-\text{C}$ . Therefore, the directional electron transfer takes place from the CoNi alloy to the  $\text{Fe}-\text{N}-\text{C}$  support via the Co/Ni–N bridging bond, along with the electron transfer from Fe to C and N at the atomic scale in the  $\text{Fe}-\text{N}-\text{C}$  support. The directional electron transfer behavior in  $\text{Co}_{0.66}\text{Ni}_{0.34}@\text{Fe}-\text{N}-\text{C}$  can accelerate the charge transfer from CoNi alloys to the carbon and pyridinic N and increase the electron utilization efficiency of electrons in the electrocatalytic reaction, thereby improving bifunctional electrocatalytic performance.<sup>[29,30]</sup>

## 2.2. Bifunctional Electrocatalytic Performance

To confirm the benefits of the developed directional electron transfer mechanism, the electrocatalytic ORR performance of  $\text{Co}_{0.66}\text{Ni}_{0.34}@\text{Fe}-\text{N}-\text{C}$  was evaluated and compared to those of  $\text{Co}_{0.66}\text{Ni}_{0.34}@\text{C}$ ,  $\text{Fe}-\text{N}-\text{C}$ ,  $\text{Ni}@\text{Fe}-\text{N}-\text{C}$ ,  $\text{Co}@\text{Fe}-\text{N}-\text{C}$ , and commercial Pt/C. Analysis of the CV curves in Figure 4a shows that all six materials display distinct cathodic peaks when present in  $\text{O}_2$ -saturated 0.1 M KOH solutions, while no cathodic peaks exist in the profiles of the materials in the  $\text{N}_2$ -saturated solutions. These observations demonstrate that all these materials

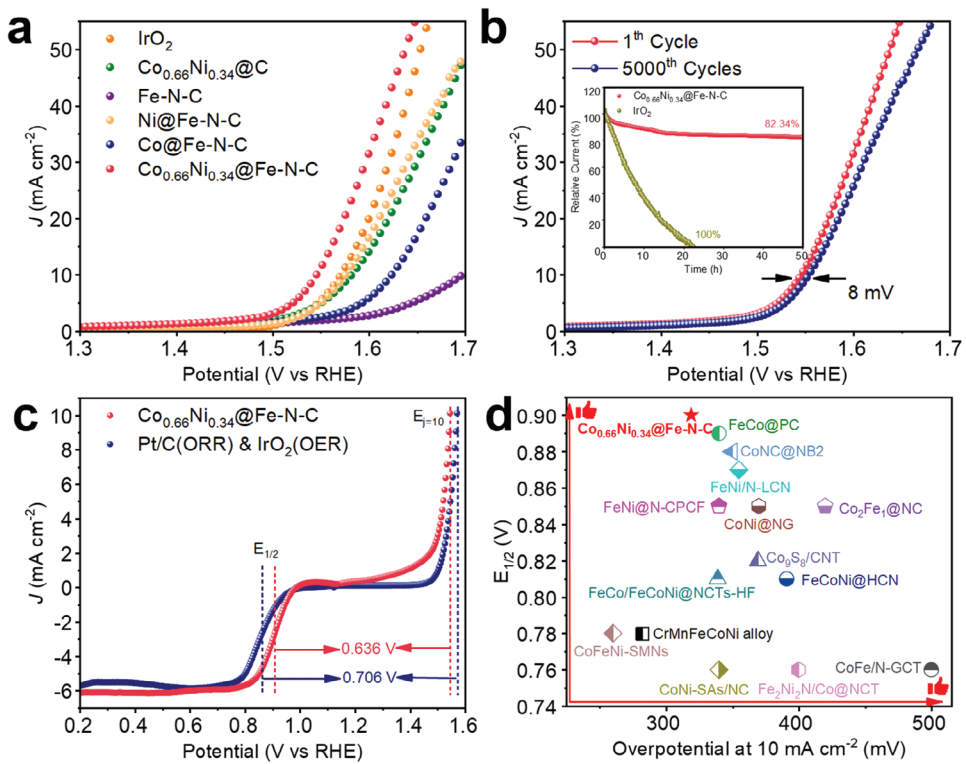


**Figure 5.** Evaluation of bifunctional electrocatalytic performance for the OER. a) LSV curves in 1 M KOH solution. b) Stability test for the OER. c) Bifunctional ORR/OER polarization curves. d) Comparison with the bifunctional electrocatalytic performance of non-noble catalysts.

have ORR activity. The reduction peak for  $\text{Co}_{0.66}\text{Ni}_{0.34}@\text{Fe}-\text{N}-\text{C}$  has a potential of 0.87 V (vs RHE), which is higher than those of  $\text{Co}_{0.66}\text{Ni}_{0.34}@\text{C}$  (0.76 V),  $\text{Fe}-\text{N}-\text{C}$  (0.86 V) and  $\text{Ni}@\text{Fe}-\text{N}-\text{C}$  (0.85 V). This value indicates that  $\text{Co}_{0.66}\text{Ni}_{0.34}@\text{Fe}-\text{N}-\text{C}$  displays an enhanced ORR catalytic performance. The LSV curves in Figure 4b, show that  $\text{Co}_{0.66}\text{Ni}_{0.34}@\text{Fe}-\text{N}-\text{C}$  electrocatalyst has a higher onset potential ( $E_{\text{onset}}$ ) of 1.02 V and half-wave potential ( $E_{1/2}$ ) of 0.90 V compared to those of other electrocatalysts. Notably, the  $E_{1/2}$  of  $\text{Co}_{0.66}\text{Ni}_{0.34}@\text{Fe}-\text{N}-\text{C}$  is even higher than that of the commercial Pt/C. These observations indicate that the enhanced ORR activity of  $\text{Co}_{0.66}\text{Ni}_{0.34}@\text{Fe}-\text{N}-\text{C}$  is mainly due to the presence of a highly efficient electron transfer pathway occurring at the heterogeneous interface between CoNi alloys to a pyridinic N in the support. In effect, the directional electron transfer mechanism adjusts the electronic state of the catalyst, implying that the adsorption energies of oxygen-containing species, such as  $^{\bullet}\text{O}$  and  $^{\bullet}\text{OH}$ , can be modulated. It also functions as a preferable activation route for these oxygen-containing species, which can accelerate the ORR process.<sup>[31]</sup> Moreover,  $\text{Co}_{0.66}\text{Ni}_{0.34}@\text{Fe}-\text{N}-\text{C}$  has the highest percentage of pyridinic N than  $\text{Co}_{0.24}\text{Ni}_{0.76}@\text{Fe}-\text{N}-\text{C}$ ,  $\text{Co}_{0.34}\text{Ni}_{0.66}@\text{Fe}-\text{N}-\text{C}$ ,  $\text{Co}_{0.50}\text{Ni}_{0.50}@\text{Fe}-\text{N}-\text{C}$ , and  $\text{Co}_{0.76}\text{Ni}_{0.24}@\text{Fe}-\text{N}-\text{C}$ . (Figure S15 and Table S3, Supporting Information), which shows the best ORR catalytic performance (Figures S16–S19, Supporting Information).<sup>[32]</sup> Another factor involved in enhancing the ORR performance of  $\text{Co}_{0.66}\text{Ni}_{0.34}@\text{Fe}-\text{N}-\text{C}$  is that this material has a high diffusion limiting current density ( $J_{\text{L}}$ ) ( $-6.15 \text{ mA cm}^{-2}$ ) that is even higher than that of commercial Pt/C ( $-5.51 \text{ mA cm}^{-2}$ ). The reason for this is the excellent electroconductivity of

the graphitized  $\text{Fe}-\text{N}-\text{C}$  support and efficient electron transfer pathway at the spatial heterostructure.<sup>[33]</sup>

The kinetics of electron transfer in the ORR for  $\text{Co}_{0.66}\text{Ni}_{0.34}@\text{Fe}-\text{N}-\text{C}$  were evaluated using LSV at various rotation rates on the rotating disk electrode (RDE). According to the Koutecky-Levich equation,  $\text{Co}_{0.66}\text{Ni}_{0.34}@\text{Fe}-\text{N}-\text{C}$  has an electron-transfer number of ca. 4, which is higher than those of the control materials. This indicates that the ORR catalyzed by this material takes place through a four-electron pathway (Figure 4c; Figures S20 and S21, Supporting Information). A chronoamperometric (CA) test was carried out on  $\text{Co}_{0.66}\text{Ni}_{0.34}@\text{Fe}-\text{N}-\text{C}$  for 16 h to determine its robustness during the ORR (Figure 4d; Figure S22, Supporting Information). The results indicate that this electrocatalyst maintains a high current retention (ca. 88.65%) during the stability test. In contrast, Pt/C displays a significant activity decline associated with a current retention of only ca. 62.47% during the same time period. Moreover, the excellent stability of  $\text{Co}_{0.66}\text{Ni}_{0.34}@\text{Fe}-\text{N}-\text{C}$  by the negligible 11 mV decrease that occurs in the half-wave potential during the ORR after 5000 CV cycles. The excellent stability is likely caused by the robustness of the  $\text{Fe}-\text{N}-\text{C}$  support and an anchoring effect on metal nanoparticles through the coordination of Co/Ni and N.<sup>[34]</sup>

$\text{Co}_{0.66}\text{Ni}_{0.34}@\text{Fe}-\text{N}-\text{C}$  displays good performance as a catalyst for the OER. The profiles in Figure 5a show that  $\text{Co}_{0.66}\text{Ni}_{0.34}@\text{Fe}-\text{N}-\text{C}$  requires an overpotential of only 317 mV to deliver a current density of  $10 \text{ mA cm}^{-2}$  in the OER in 1.0 M KOH. This value is lower than those of  $\text{Co}_{0.66}\text{Ni}_{0.34}@\text{C}$  (354 mV),  $\text{Fe}-\text{N}-\text{C}$  (467 mV),  $\text{Ni}@\text{Fe}-\text{N}-\text{C}$  (347 mV),  $\text{Co}@\text{Fe}-\text{N}-\text{C}$

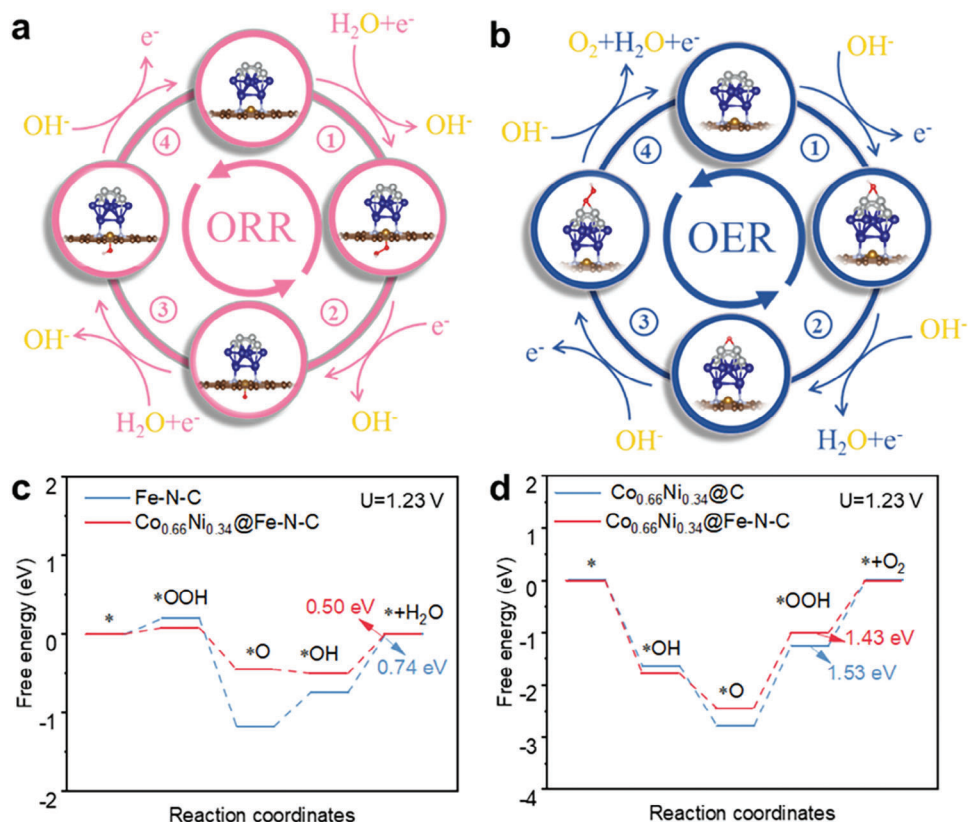


**Figure 6.** a,b) The ORR and OER (shown clockwise) mechanisms over Co<sub>0.66</sub>Ni<sub>0.34</sub>@Fe—N—C. c) The calculated free energy diagrams for the ORR pathway of Co<sub>0.66</sub>Ni<sub>0.34</sub>@Fe—N—C and Fe—N—C catalysts. d) The calculated free energy diagrams for the OER pathway of Co<sub>0.66</sub>Ni<sub>0.34</sub>@Fe—N—C and Co<sub>0.66</sub>Ni<sub>0.34</sub>@C catalysts.

(395 mV), and commercial IrO<sub>2</sub> (342 mV). The electrochemical active surface area (ECSA) on Co<sub>0.66</sub>Ni<sub>0.34</sub>@Fe—N—C was evaluated by using double-layer capacitance (C<sub>dl</sub>) measurements arising from CV at different scan rates (Figure S23, Supporting Information). Notably, Co<sub>0.66</sub>Ni<sub>0.34</sub>@Fe—N—C exhibits a much higher C<sub>dl</sub> value of 34.87 mF cm<sup>-2</sup> compared to other materials, indicating its abundant active sites and large ECSA. It can be attributed to alloying and exposure of more active sites by introducing Fe—N—C supports. (Figure S24, Supporting Information). Electrochemical impedance spectroscopy (EIS) was used to examine the charge transfer behavior during the OER. The Nyquist plots shown in Figure S25 (Supporting Information) indicate that Co<sub>0.66</sub>Ni<sub>0.34</sub>@Fe—N—C promotes a more efficient charge transfer process than the control materials, as evidenced by a lower charge transfer resistance. Due to a smaller Tafel slope (Figure S26, Supporting Information), Co<sub>0.66</sub>Ni<sub>0.34</sub>@Fe—N—C catalyzes a more rapid OER than Co<sub>0.66</sub>Ni<sub>0.34</sub>@C, Fe—N—C, and Co@Fe—N—C. This finding suggests that the highest proportion of metallic Ni<sup>0</sup> and Co<sup>0</sup> in an optimal Co/Ni ratio of 1/2 leads to exposure of more metal-active sites, which is beneficial to the ECSA and OER kinetics (Figures S27–S30 and Table S4, Supporting Information).<sup>[35,36]</sup> Hence, Co<sub>0.66</sub>Ni<sub>0.34</sub>@Fe—N—C also has a higher OER activity compared to those of Co<sub>0.24</sub>Ni<sub>0.76</sub>@Fe—N—C, Co<sub>0.34</sub>Ni<sub>0.66</sub>@Fe—N—C, Co<sub>0.50</sub>Ni<sub>0.50</sub>@Fe—N—C and Co<sub>0.76</sub>Ni<sub>0.24</sub>@Fe—N—C (Figures S31–S34, Supporting Information). Furthermore, the existence of more active sites on the

surface facilitates the binding and transport of a greater number of protons,<sup>[37]</sup> and the higher directional charge transfer propensity at heterogeneous interfaces enhances the electron transfer efficiency and decreases charge transfer impedance. In addition, the optimal electronic configuration of CoNi alloys enables regulation and optimization of the Gibbs free energy for water adsorption, which leads to enhanced OER performance in an alkaline medium.<sup>[21]</sup> The robustness of Co<sub>0.66</sub>Ni<sub>0.34</sub>@Fe—N—C for OER is assessed using cyclic voltammetry (CV) and chronoamperometry (CA) tests (Figure 5b). It shows that the catalyst experiences a minimal increase of ca. 8 mV in the overpotential at a current density of 10 mA cm<sup>-2</sup> after 5000 CV cycles. Furthermore, Co<sub>0.66</sub>Ni<sub>0.34</sub>@Fe—N—C displays high stability during the OER with a high current retention of ca. 82.34% after the 50 h operation. In contrast, commercial IrO<sub>2</sub> experiences significant activity degradation during the same tests (Figure 5b; Figure S35, Supporting Information). Differences ( $\Delta E$ ) between the ORR potential at half-wave potential (E<sub>1/2</sub>) and the OER potential at 10 mA cm<sup>-2</sup> (E<sub>j=10</sub>) were employed to evaluate the bifunctional electrocatalytic activity of Co<sub>0.66</sub>Ni<sub>0.34</sub>@Fe—N—C. The process promoted by Co<sub>0.66</sub>Ni<sub>0.34</sub>@Fe—N—C has a lower  $\Delta E$  value of 0.636 V compared to those of Pt/C and IrO<sub>2</sub> (Figure 5c) indicating that it has a better bifunctional catalytic performance. It is worth mentioning that Co<sub>0.66</sub>Ni<sub>0.34</sub>@Fe—N—C outperforms the state-of-the-art non-noble catalysts listed in Table S6 (Supporting Information) and Figure 5d.

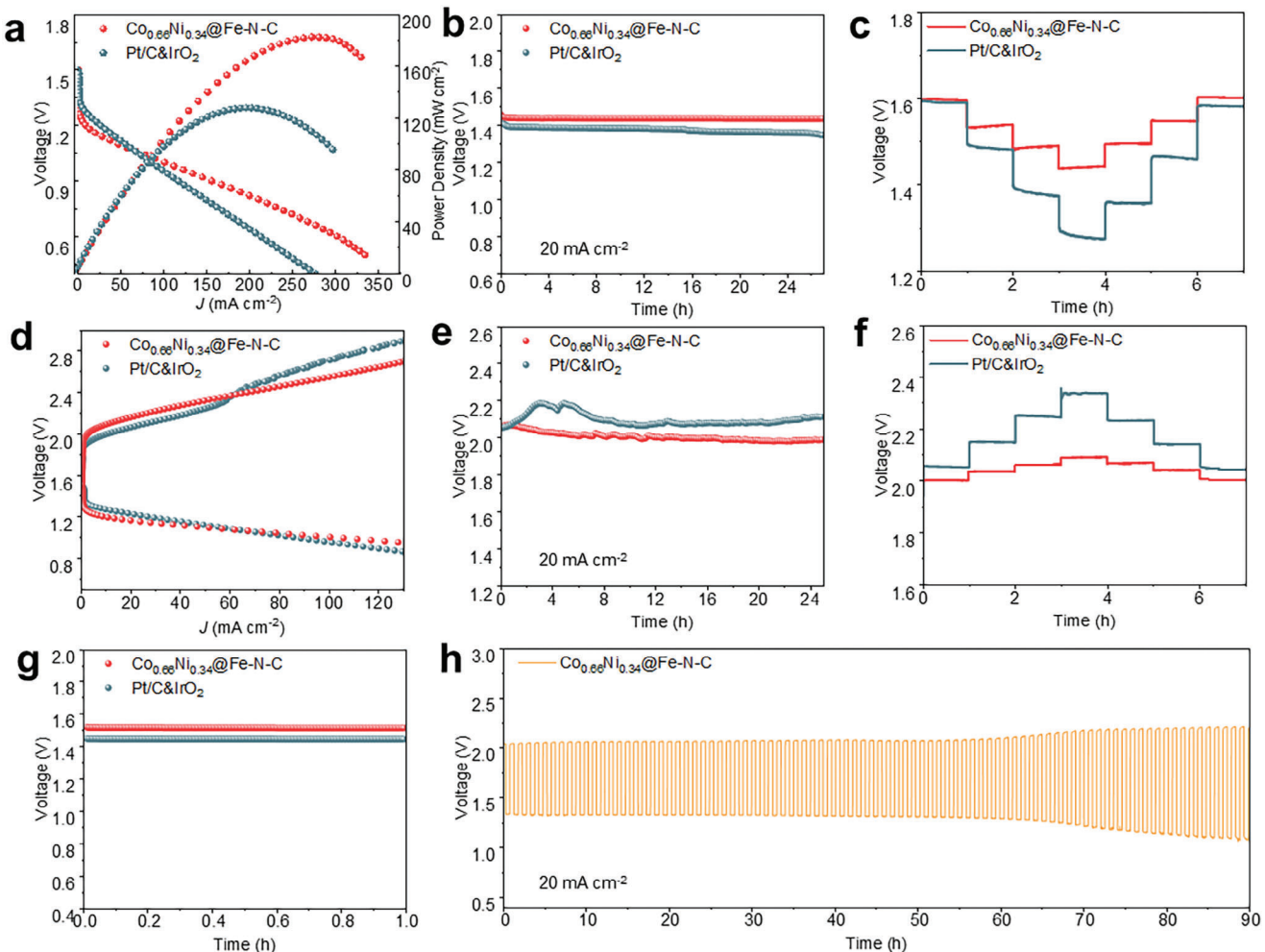


**Figure 7.** The performance of liquid Zn–air battery assembled using  $\text{Co}_{0.66}\text{Ni}_{0.34}@\text{Fe}-\text{N}-\text{C}$  as the air cathode. a) Polarization and power density curves. b) Long-term galvanostatic discharging curves at  $20 \text{ mA cm}^{-2}$ . c) Rate performance for discharging at different current densities. d) Charge–discharge polarization curves. e) Long-term galvanostatic charging curves at  $20 \text{ mA cm}^{-2}$ . f) Rate performance for charging at different current densities. g) Open-circuit potential (OCP) for assembled ZABs. (h) Discharge-charge cycling stability at  $20 \text{ mA cm}^{-2}$ .

### 2.3. DFT Calculations for the OER/ORR Mechanism

To gain deeper insights into the crucial role of the directional electron transfer mechanism between CoNi alloys and Fe–N–C support for OER and ORR, density functional theory (DFT) calculations were performed to reveal the energetically favorable pathway for ORR and OER. The proposed ORR/OER mechanisms of  $\text{Co}_{0.66}\text{Ni}_{0.34}@\text{Fe}-\text{N}-\text{C}$  are illustrated in Figure 6a,b. The active sites of ORR were selected by pre-adsorbing oxygen intermediates ( $\text{O}^*$ ,  $\text{OH}^*$ , and  $\text{OOH}^*$ ) on Fe–N–C sites. When no potential is applied ( $U = 0 \text{ V}$ ), the catalysts exhibit a down-hill pathway for the ORR process (Figure S36, Supporting Information). Interestingly, by constructing the directional electron transfer pathway, the free energy of  $\text{O}^*$  significantly increased. The process of transition from  $\text{O}^*$  to  $\text{OH}^*$  converts from an endothermic process to an exothermic process. Additionally, the rate-determining step (RDS) of the process from  $\text{OH}^*$  to  $\text{H}_2\text{O}$  shows a decreased free energy change ( $\Delta G$ ) from 0.74 to 0.50 eV (Figure 6c).

For OER, the free energy of intermediates was calculated on  $\text{Co}_{0.66}\text{Ni}_{0.34}@\text{Fe}-\text{N}-\text{C}$  and  $\text{Co}_{0.66}\text{Ni}_{0.34}@\text{C}$ . Wherein, alloy nanoparticles serve as reaction sites. The conversion of  $\text{O}^*$  to  $\text{OOH}^*$ , and  $\text{OOH}^*$  to  $\text{O}_2^*$  were endothermic and thermodynamically unfavorable processes with  $\Delta G$  of 1.53 and 1.25 eV for  $\text{Co}_{0.66}\text{Ni}_{0.34}@\text{C}$ . However, after introducing Fe and N heteroatoms into support and reducing the electronegativity of the support, the  $\Delta G$  of both processes has decreased. Especially for RDS, which involves  $\text{O}^*$  to  $\text{OOH}^*$ ,  $\Delta G$  is merely 1.43 eV (Figure 6d). Thus, both experimental and theoretical results point to the critical role of the directional electron transfer between CoNi alloys and Fe–N–C support, which could potentially reduce the ORR/OER barrier and accelerate the catalytic kinetics.<sup>[31,38]</sup>

### 2.4. Rechargeable Zn–Air Battery Performance

To determine if the outstanding bifunctional catalytic activity of  $\text{Co}_{0.66}\text{Ni}_{0.34}@\text{Fe}-\text{N}-\text{C}$  is reflected in the function of a

practical battery, a homemade rechargeable Zn-air battery was assembled. The battery is comprised of a zinc plate as the anode,  $\text{Co}_{0.66}\text{Ni}_{0.34}@\text{Fe}-\text{N}-\text{C}$  as the air-cathode, and 6.0 M KOH / 0.2 M  $\text{Zn}(\text{CH}_3\text{COO})_2$  as the electrolyte. The polarization curves in Figure 7a show that the liquid zinc-air battery containing  $\text{Co}_{0.66}\text{Ni}_{0.34}@\text{Fe}-\text{N}-\text{C}$  has a higher maximum discharge power density (182.7 mW  $\text{cm}^{-2}$  at 281.1 mA  $\text{cm}^{-2}$ ) than a battery assembled using  $\text{Pt/C} \parallel \text{IrO}_2$  (127.8 mW  $\text{cm}^{-2}$  at 200.3 mA  $\text{cm}^{-2}$ ). Moreover, the observation that a  $\text{Co}_{0.66}\text{Ni}_{0.34}@\text{Fe}-\text{N}-\text{C}$  assembled ZAB has a charge-discharge voltage gap comparable to a  $\text{Pt/C} \parallel \text{IrO}_2$  assembled battery, indicates that the former has an excellent bifunctional electrocatalytic activity under practical operating conditions (Figure 7d). The Zn-air battery containing  $\text{Co}_{0.66}\text{Ni}_{0.34}@\text{Fe}-\text{N}-\text{C}$  also has high stability, reflected by the minimal voltage fluctuations occurring during 27 h of galvanostatic discharge at 20 mA  $\text{cm}^{-2}$  (Figure 7b). During the galvanostatic charging process, the  $\text{Pt/C} \parallel \text{IrO}_2$  assemble battery exhibits a higher charging potential (2.14 V) with a significant variation in voltage, which contrasts with the  $\text{Co}_{0.66}\text{Ni}_{0.34}@\text{Fe}-\text{N}-\text{C}$  analog which has high robustness reflected in the finding that no significant degradation of charging potential (2.01 V) takes place even after 27 h of galvanostatic charging at 20 mA  $\text{cm}^{-2}$  (Figure 7e). The rate performance of the  $\text{Co}_{0.66}\text{Ni}_{0.34}@\text{Fe}-\text{N}-\text{C}$  assembled ZAB was tested utilizing different current densities (5, 10, 15, 20, 15, 10, and 5 mA  $\text{cm}^{-2}$ ) for the charging and discharging processes. The results show that the  $\text{Co}_{0.66}\text{Ni}_{0.34}@\text{Fe}-\text{N}-\text{C}$  assembled ZAB performs better than the  $\text{Pt/C} \parallel \text{IrO}_2$  counterpart (Figure 7c,f). Finally, the  $\text{Co}_{0.66}\text{Ni}_{0.34}@\text{Fe}-\text{N}-\text{C}$  air cathode can power a small fan (Figure S37, Supporting Information) and has an open-circuit potential (OCP) of 1.51 V, which is higher than that of Pt/C (1.45 V) (as shown in Figure 7g). Furthermore, the cathode has high stability during discharge-charge cycling over 60 h at a current density of 20 mA  $\text{cm}^{-2}$ . This contrasts with the ZAB assembled using  $\text{Pt/C} \parallel \text{IrO}_2$ , which experiences a significant voltage increase after 20 h at 20 mA  $\text{cm}^{-2}$  (Figure 7h; Figure S38, Supporting Information). A comparison of the performance of the  $\text{Co}_{0.66}\text{Ni}_{0.34}@\text{Fe}-\text{N}-\text{C}$ -based ZAB to those of various liquid ZABs is given in Table S6 (Supporting Information).<sup>[39,40]</sup>

### 3. Conclusion

In conclusion, a spatial junction  $\text{Co}_y\text{Ni}_x@\text{Fe}-\text{N}-\text{C}$  was fabricated by using a solvothermal reaction and post-pyrolysis process. Due to the existence of a directional electron transfer pathway created by strong coupling of the Co/Ni alloy with the Fe–N–C support through the cobalt/nickel-nitrogen bond (Co/Ni–N),  $\text{Co}_y\text{Ni}_x@\text{Fe}-\text{N}-\text{C}$  has enhanced electroconductivity and electrocatalytic activity in the ORR and OER. Also, it was shown that  $\text{Co}_{0.66}\text{Ni}_{0.34}@\text{Fe}-\text{N}-\text{C}$  with an optimal Ni/Co ratio has an ORR performance that is superior to that of commercial Pt/C. For the ORR in 0.1 M KOH, the new electrocatalyst has an onset potential of 1.02 V, a half-wave potential of 0.90 V, and a high limiting current density of  $-6.15 \text{ mA cm}^{-2}$ .  $\text{Co}_{0.66}\text{Ni}_{0.34}@\text{Fe}-\text{N}-\text{C}$  also has an outstanding OER performance in 1 M KOH compared to those of control materials, requiring only 317 mV of overpotential to deliver 10 mA  $\text{cm}^{-2}$  current density. Additionally, a  $\text{Co}_{0.66}\text{Ni}_{0.34}@\text{Fe}-\text{N}-\text{C}$ -based zinc-air battery has a high and stable open circuit potential (1.51 V), peak power density

of 182.72 mW  $\text{cm}^{-2}$ , and good discharge-charge cycling stability over 60 h at a current density of 20 mA  $\text{cm}^{-2}$ . The results of the effort show that the bifunctional electrocatalytic electrocatalytic activity of a heterostructured material for the OER and ORR can be elevated by incorporation of an effective directed electron transfer channel to improve the electron utilization efficiency. Moreover, electrocatalysts generated utilizing this general design strategy can be applied to construction of a functioning rechargeable Zn-air battery.

### 4. Experimental Section

**Materials:** The hemin was purchased from Shanghai Macklin Biochemical Technology Co., Ltd. with a purity of  $\geq 99.99\%$ . Melamine and ammonium chloride were obtained from Sinopharm Chemical Reagent Co., Ltd. with a purity of AR and  $\geq 98\%$ , respectively. 2,5-dihydroxyterephthalic acid, cobalt nitrate hexahydrate, and nickel acetate tetrahydrate with a purity of AR and  $\geq 98.5\%$  were bought from Aladdin Industrial Corporation. Yttrium dioxide with a purity of AR and  $\geq 99.99\%$  was obtained from Shaanxi Kaida Chemical Co., Ltd. Johnson Matthey provided the commercial 20 wt% Pt/Ct. All the water used in the experiment was self-made and deionized with a resistance of  $18.25 \text{ M}\Omega \text{ cm}^{-1}$ .

**Synthesis of  $\text{Fe}-\text{N}-\text{C}$ :** To prepare  $\text{Fe}-\text{N}-\text{C}$ , 1.0 g of Melamine and 0.2 g of Hemin were ground together in a mortar for 30 min. The resulting mixture was then placed in a porcelain boat and calcined in an Ar atmosphere for 2 h at 900 °C, with a heating rate of 5 °C·min $^{-1}$ . A porcelain boat filled with ammonium chloride was placed at the tube intake end of the furnace. The final product obtained was a black powder, which was denoted as  $\text{Fe}-\text{N}-\text{C}$ .

**Synthesis of  $\text{Co}_y\text{Ni}_x\text{-MOF-74}@\text{Fe}-\text{N}-\text{C}$  ( $x + y = 1$ ):** X millimoles of Cobalt nitrate hexahydrate and Y millimoles of Nickel acetate tetrahydrate, along with 100 milligrams of  $\text{Fe}-\text{N}-\text{C}$  and 40 mg of 2,5-Dihydroxyterephthalic acid, were added to a mixed solution of DMF, ethanol and  $\text{H}_2\text{O}$  in a volume ratio of 15:1:1. The mixture was then dispersed using ultrasound for 2.5 h, followed by a solvothermal reaction at 120 °C for 24 h. The resulting mixture was centrifuged and washed several times with a mixed solution of ethanol and deionized water, and the sample was vacuum-dried to obtain a tan powder, which was named  $\text{Co}_y\text{Ni}_x\text{-MOF-74}@\text{Fe}-\text{N}-\text{C}$ .

**Synthesis of  $\text{Co}_y\text{Ni}_x@\text{Fe}-\text{N}-\text{C}$  ( $x + y = 1$ ):** The  $\text{Co}_y\text{Ni}_x\text{-MOF-74}@\text{Fe}-\text{N}-\text{C}$  ( $x + y = 1$ ) was heated in a porcelain boat at 600 °C with a heating rate of 5 °C·min $^{-1}$  for 2 h in a mixed atmosphere of 5%  $\text{H}_2/\text{Ar}$ . After the process, a black powder was obtained which was named  $\text{Co}_y\text{Ni}_x@\text{Fe}-\text{N}-\text{C}$ . Similarly,  $\text{Co}@\text{Fe}-\text{N}-\text{C}$  and  $\text{Ni}@\text{Fe}-\text{N}-\text{C}$  were synthesized by following the same procedure, except that the Ni source and Co source were not added, respectively.

### Supporting Information

Supporting Information is available from the Wiley Online Library or from the author.

### Acknowledgements

This work was supported by the Guangdong Key R&D Project (2020B0909040001) and the National Natural Science Foundation of China (22279096).

### Conflict of Interest

The authors declare no conflict of interest.

## Author Contributions

Z.X. and S.W. contributed equally to this work. This manuscript was written through contributions made by all authors. All authors have approved the final version of the manuscript.

## Data Availability Statement

The data that support the findings of this study are available from the corresponding author upon reasonable request.

## Keywords

bifunctional electrocatalysts, directional electron transfer, rechargeable zinc–air battery, spatial heterostructure, stoichiometric regulation

Received: March 5, 2024

Revised: June 27, 2024

Published online: July 22, 2024

- [1] H. Xie, Z. Zhao, T. Liu, Y. Wu, C. Lan, W. Jiang, L. Zhu, Y. Wang, D. Yang, Z. Shao, *Nature* **2022**, 612, 673.
- [2] T. Ma, J. L. Lutkenhaus, *Science* **2022**, 378, 138.
- [3] P. Chen, K. Y. Zhang, D. J. Tang, W. L. Liu, F. C. Meng, Q. W. Huang, J. H. Liu, *Front. Chem.* **2020**, 8, 7.
- [4] Y. X. Wang, J. X. Liu, T. Lu, R. He, N. N. Xu, J. L. Qiao, *Appl. Catal. B-Environ.* **2023**, 321, 122041.
- [5] T. Liu, J. R. Mou, Z. P. Wu, C. Lv, J. L. Huang, M. L. Liu, *Adv. Funct. Mater.* **2020**, 30, 9.
- [6] Z. Q. Zhao, X. Y. Fan, J. Ding, W. B. Hu, C. Zhong, J. Lu, *ACS Energy Lett.* **2019**, 4, 2259.
- [7] C. S. Li, Y. Sun, F. Gebert, S. L. Chou, *Adv. Energy Mater.* **2017**, 7, 11.
- [8] X. L. Lang, Z. B. Hu, C. Y. Wang, *Chin. Chem. Lett.* **2021**, 32, 999.
- [9] D. Böhm, M. Beetz, M. Schuster, K. Peters, A. G. Hufnagel, M. Döblinger, B. Böller, T. Bein, D. Fattakhova-Rohlfing, *Adv. Funct. Mater.* **2020**, 30, 14.
- [10] P. Li, F. Q. Qiang, X. H. Tan, Z. Li, J. Shi, S. Liu, M. H. Huang, J. W. Chen, W. Q. Tian, J. Y. Wu, W. Hu, H. L. Wang, *Appl. Catal. B-Environ.* **2024**, 340, 12.
- [11] M. J. Wu, G. X. Zhang, Y. F. Hu, J. Wang, T. X. Sun, T. Regier, J. L. Qiao, S. H. Sun, *Carbon Ener.* **2021**, 3, 176.
- [12] J. Li, M. Chen, D. A. Cullen, S. Hwang, M. Wang, B. Li, K. Liu, S. Karakalos, M. Lucero, H. Zhang, *Nat. Catal.* **2018**, 1, 935.
- [13] Y. Wang, H. Su, Y. He, L. Li, S. Zhu, H. Shen, P. Xie, X. Fu, G. Zhou, C. Feng, *Chem. Rev.* **2020**, 120, 12217.
- [14] M. Zhao, H. Liu, H. Zhang, W. Chen, H. Sun, Z. Wang, B. Zhang, L. Song, Y. Yang, C. Ma, *Energy Environ. Sci.* **2021**, 14, 6455.
- [15] H. Jin, J. Wang, D. Su, Z. Wei, Z. Pang, Y. Wang, *J. Am. Chem. Soc.* **2015**, 137, 2688.
- [16] P. Chen, K. Xu, Z. Fang, Y. Tong, J. Wu, X. Lu, X. Peng, H. Ding, C. Wu, Y. Xie, *Angew. Chem., Int. Ed.* **2015**, 127, 14923.
- [17] G. Hou, X. Jia, H. Kang, X. Qiao, Y. Liu, Y. Li, X. Wu, W. Qin, *Appl. Catal. B-Environ.* **2022**, 315, 121551.
- [18] T. Chen, F. Wang, S. Cao, Y. Bai, S. Zheng, W. Li, S. Zhang, S. X. Hu, H. Pang, *Adv. Mater.* **2022**, 34, 2201779.
- [19] P. Li, F. Qiang, X. Tan, Z. Li, J. Shi, S. Liu, M. Huang, J. Chen, W. Tian, J. Wu, *Appl. Catal. B-Environ.* **2024**, 340, 123231.
- [20] X. Wang, H. Xiao, A. Li, Z. Li, S. Liu, Q. Zhang, Y. Gong, L. Zheng, Y. Zhu, C. Chen, *J. Am. Chem. Soc.* **2018**, 140, 15336.
- [21] Y. Liu, Z. Chen, Z. Li, N. Zhao, Y. Xie, Y. Du, J. Xuan, D. Xiong, J. Zhou, L. Cai, *Nano Energy* **2022**, 99, 107325.
- [22] W. Xiong, H. Li, H. You, M. Cao, R. Cao, *Natl. Sci. Rev.* **2020**, 7, 609.
- [23] A. Zhang, Y. Liang, H. Zhang, Z. Geng, J. Zeng, *Chem. Soc. Rev.* **2021**, 50, 9817.
- [24] G. Zhao, Y. Jiang, S.-X. Dou, W. Sun, H. Pan, *Sci. Bull.* **2021**, 66, 85.
- [25] S. Wang, H. Pan, Y. Wang, H. Tang, H. Zhang, *Small Struct.* **2024**, 5, 2400031.
- [26] L. J. Zhang, H. Jang, H. H. Liu, M. G. Kim, D. J. Yang, S. G. Liu, X. E. Liu, J. Cho, *Angew. Chem.-Int. Edit.* **2021**, 60, 18821.
- [27] L. Peng, J. Yang, Y. Yang, F. Qian, Q. Wang, D. Sun-Waterhouse, L. Shang, T. Zhang, G. I. Waterhouse, *Adv. Mater.* **2022**, 34, 2202544.
- [28] S. Anantharaj, S. Kundu, S. Noda, *Nano Energy* **2021**, 80, 105514.
- [29] D. Ding, K. Shen, X. Chen, H. Chen, J. Chen, T. Fan, R. Wu, Y. Li, *ACS Catal.* **2018**, 8, 7879.
- [30] Y. Zhou, H. Liu, X. Gu, X. Wu, L. Feng, *Carbon Energy* **2022**, 4, 924.
- [31] Q. Lu, H. Wu, X. Zheng, Y. Chen, A. L. Rogach, X. Han, Y. Deng, W. Hu, *Adv. Sci.* **2021**, 8, 2101438.
- [32] B. Zhu, Z. Liang, D. Xia, R. Zou, *Energy Stor. Mater.* **2019**, 23, 757.
- [33] L. Ye, G. Chai, Z. Wen, *Adv. Funct. Mater.* **2017**, 27, 1606190.
- [34] X. Zhang, Y. B. Mollamahale, D. Lyu, L. Liang, F. Yu, M. Qing, Y. Du, X. Zhang, Z. Q. Tian, P. K. Shen, *J. Catal.* **2019**, 372, 245.
- [35] L. Shen, J. Ying, K. I. Ozoemena, C. Janiak, X. Y. Yang, *Adv. Funct. Mater.* **2022**, 32, 2110851.
- [36] S. Zhang, Y. Hao, D. Su, V. V. Doan-Nguyen, Y. Wu, J. Li, S. Sun, C. B. Murray, *J. Am. Chem. Soc.* **2014**, 136, 15921.
- [37] S. Wang, M. Fan, H. Pan, J. Lyu, J. Wu, H. Tang, H. Zhang, *J. Energy Chem.* **2024**, 96, 526.
- [38] Y. Liu, L. Zhou, S. Liu, S. Li, J. Zhou, X. Li, X. Chen, K. Sun, B. Li, J. Jiang, *Angew. Chem., Int. Ed.* **2024**, 136, 202319983.
- [39] K. Srinivas, Z. Chen, F. Ma, A. Chen, Z. Zhang, Y. Wu, M.-q. Zhu, Y. Chen, *Appl. Catal. B-Environ.* **2023**, 335, 122887.
- [40] R. He, L. Yang, Y. Zhang, D. Jiang, S. Lee, S. Horta, Z. Liang, X. Lu, A. O. Moghaddam, J. Li, *Adv. Mater.* **2023**, 35, 2303719.